

Enhanced Directional Light Extraction from Patterned Rare-Earth Phosphor Films

Elena Cabello-Olmo, Pau Molet, Agustín Mihi,* Gabriel Lozano,* and Hernán Míguez

The combination of light-emitting diodes (LEDs) and rare earth (RE) phosphors as color-converting layers comprises the basis of solid-state lighting. Indeed, most LED lamps include a photoluminescent coating made of phosphor material, i.e., crystalline matrix suitably doped with RE elements, to produce white light from a blue or ultraviolet LED chip. Transparent phosphor-based films constitute starting materials for new refined emitters that allow different photonic designs to be implemented. Among the different photonic strategies typically employed to tune or enhance emission, surface texturing has proved its versatility and feasibility in a wide range of materials and devices. However, most of the nanofabrication techniques cannot be applied to RE phosphors directly because of their chemical stability or because of their cost. The first monolithic patterned structure of down-shifting nanophosphors with square arrays of nanoholes with different lattice parameters is reported in this study. It is shown that a low-cost soft-nanolithography procedure can be applied to red-emitting nanophosphors ($\text{GdVO}_4\text{:Eu}^{3+}$ nanocrystals) to tune their emission properties, attaining a twofold directional enhancement of the emitted light at predesigned emission wavelengths in specific directions.

Light out-coupling is a key point for every light-emitting system since light is generally generated in a medium with high refractive index, and thus a significant fraction of the emitted light, regardless of the internal efficiency of the emitter, will remain trapped in the emitting layer. This drastically affects the external quantum efficiency of the devices. Several out-coupling strategies have been developed in the last years to alleviate this drawback. Optimized devices typically feature microlenses,^[1–3] scattering layers,^[4,5] surface roughening, and ^[6] dielectric or

even metallic periodic arrays^[7–9] to aid the emitted light escape the bulk of the device.


Phosphors are the materials most commonly used in solid-state lighting.^[10] They usually consist of inorganic matrices doped with rare-earth (RE) cations. RE phosphors offer high thermal and chemical stability and are used as color-converting materials along with blue or UV light-emitting diodes (LEDs) to obtain emissions that cover different ranges of the visible spectrum. This approach has allowed the development of artificial illumination, featuring lower cost and more efficient devices, and rendering better quality lighting for the last two decades. Apart from illumination, the field of use of LED-based devices is wide, from sensors to wireless communication, passing through human-centric lighting or horticulture industry.^[11] On this basis, directional and spectral control of the out-coupled light intensity are features of interest for many applications. Such

control could in principle be achieved in solid-state lighting by means of an adequate photonic design of the color-converting layer. However, conventional phosphor coatings in the current LED lamps are usually thick, since RE cations present low absorption cross sections, and exhibit large crystal size, giving rise to multiple scattering processes hence low transparency. As a result, directionality is nowadays attained by introducing classical optical elements, such as lenses or mirrors.

In this context, several groups have addressed the development of photon management strategies compatible with phosphor films that take advantage of the control over the optical absorption and emission they offer, and, in particular, aiming at improving the out-coupling efficiency of color-converting layers. Specifically, different photonic structures have been proposed to improve the directional and spectral control over the phosphor luminescence.^[7,12–18] Some of the preferred approaches consist in covering the phosphor layer with a 2D array of dielectric scatterers, which enhance the coupling of emitted light to free-space, mostly applied to enhance the external efficiency in both organic^[2,3] and inorganic^[19–21] LEDs. From a technical perspective, the combination of such photonic architectures with phosphor-based devices is far from compatible with most traditional lithographies. Soft-lithography, however, offers a low-cost route in the wet-processing of 2D photonic structures fully compatible with high-throughput manufacturing.^[22] In comparison with traditional photolithography, soft-lithography allows surface patterning large areas employing a variety of materials and

E. Cabello-Olmo, Dr. G. Lozano, Prof. H. Míguez
Institute of Materials Science of Seville
Spanish National Research Council—University of Seville
C/Americo Vespucio 49, Seville 41092, Spain
E-mail: g.lozano@csic.es

P. Molet, Dr. A. Mihi
Institute of Materials Science of Barcelona
Spanish National Research Council
Campus UAB, Bellaterra 08193, Spain
E-mail: amihi@icmab.es

 The ORCID identification number(s) for the author(s) of this article can be found under <https://doi.org/10.1002/adom.202001611>.

© 2020 The Authors. Advanced Optical Materials published by Wiley-VCH GmbH. This is an open access article under the terms of the Creative Commons Attribution-NonCommercial-NoDerivs License, which permits use and distribution in any medium, provided the original work is properly cited, the use is non-commercial and no modifications or adaptations are made.

DOI: 10.1002/adom.202001611

methods, with a very high reproducibility and without the limitation posed by optical diffraction.^[23,24]

In this work, we present a procedure for attaining textured phosphor films displaying enhanced directional emission properties. We developed nanophosphor pastes as starting materials that can be easily patterned by means of soft nanoimprinting lithography. The geometries of the prepatterned elastomeric stamps were chosen to maximize the intensity of selected emitted wavelengths at certain directions, compared to a flat film. After patterning and annealing, the nanophosphor films showed a twofold improvement of the photoluminescence (PL), with respect to a reference untextured film for specific targeted directions. In our, phosphor based 2D arrays, the enhancement in PL extraction takes place when Rayleigh anomalies (RAs), i.e., diffracted modes that propagate along the sample surface, match the wavelength emission characteristic of the electronic transitions of the Eu^{3+} cations. A study of the PL angular dependence along with Fourier plane spectroscopy is employed to analyse the angular dependence of the PL, the effect of the imprinted diffraction grating on the directionality of the enhancement of the emission being explicitly shown. A full theoretical description of the field distribution inside de material by finite-difference time-domain method (FDTD) is also provided to further describe the origin of the reported directional emission enhancement reported.

$\text{GdVO}_4:\text{Eu}^{3+}$ nanophosphors were synthesized following a facile solvothermal method as described in the Experimental Section. Bright luminescence in RE nanophosphors is generally achieved by choosing a matrix that allows an effective excitation of the activator through charge or energy transfer. Vanadate compounds provide such transfer, being GdVO_4 host among the ones that give rise to highest overall efficiencies. For their optical characterization, thin films were spin casted on flat, transparent, quartz substrates. A transmission electron microscopy (TEM) image of the nanoparticles employed is

shown in **Figure 1a**, where it can be appreciated that they are nearly equiaxial in shape, with a mean lateral size of 35 nm. **Figure 1b** shows the PL excitation and emission spectra of a 570 nm-thick film made of such nanophosphors. The emission spectrum exhibits the characteristic transition lines of Eu^{3+} corresponding to the relaxation from the $^5\text{D}_0$ level to $^7\text{F}_1$, $^7\text{F}_2$, $^7\text{F}_3$, and $^7\text{F}_4$. The photoexcitation targeted a broad absorption band of the host matrix in the UV and the resulting PL monitored at the most intense emission peak of Eu^{3+} , i.e., $\lambda = 619$ nm. Excitation of Eu^{3+} takes place, via a transfer mechanism, through the absorption band of the host lattice, GdVO_4 . This leads to a brighter emission, since the crystalline matrix is able to absorb the incoming light in the UV and transfer it to the RE cation. By this means, we can overcome the low absorption cross sections that the RE cations feature for $4f \rightarrow 4f$ transitions.

In order produce nanopatterned phosphor films, it is necessary to develop a nanocrystal based paste that can be nanoimprinted with elastomeric molds and that leaves a connected nanocrystal network after removal of the organic part, similarly to recent achievements with TiO_2 -based pastes.^[25,26] We prepared a viscous paste using ethyl cellulose as organic binder mixed with the nanophosphors. Transparent flat thin films acting as reference were deposited over quartz substrates, following the steps illustrated by **Figure 1c–e**. Patterned films were obtained by pressing prepatterned polydimethylsiloxane (PDMS) molds over the nanophosphors for 2 min at constant pressure over a hot surface (80 °C), as drawn in **Figure 1f**. After demolding, thermal annealing at 500 °C is used to remove any organic impurities from the synthesis or the paste and provide mechanical stability to the film. Both the flat and patterned samples are subjected to the same heating cycles for the sake of comparison. Therefore, it is not foreseen any issue regarding temperature stability when films will be combined with LEDs. Please note that annealing temperature and time determines the final emission properties (namely, PL quantum

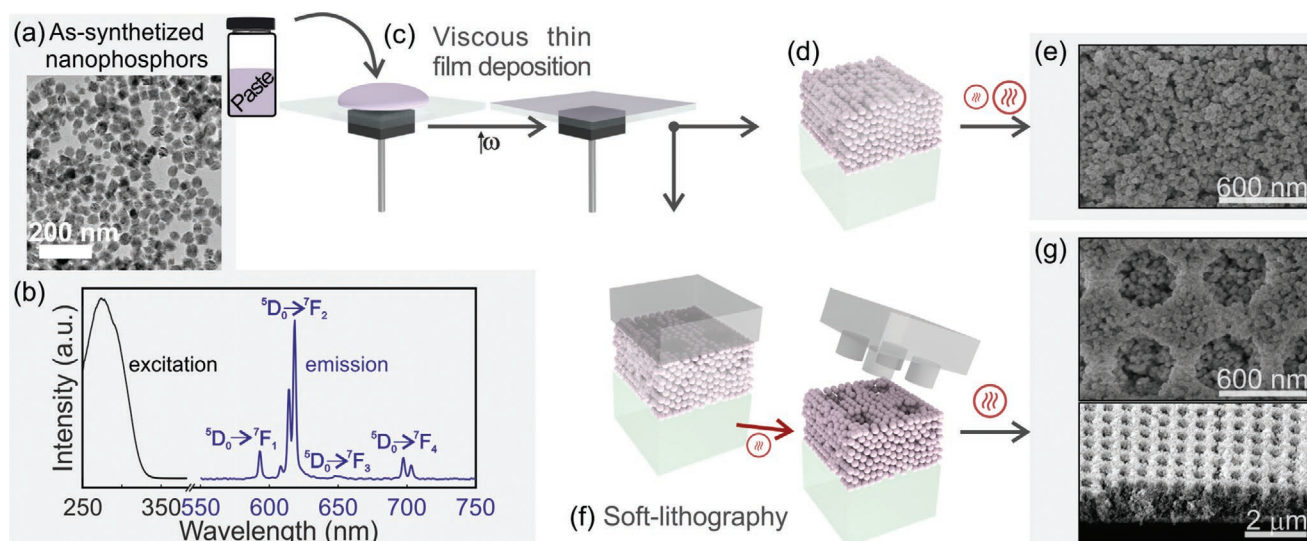


Figure 1. Schematic processing of patterned nanophosphor samples. a) TEM of the starting nanoparticles $\text{GdVO}_4:\text{Eu}^{3+}$ for the nanophosphor paste. b) Excitation (gray) and emission (blue) spectra of the synthesized nanoparticles. c) Spin coating deposition of diluted paste over a quartz substrate. d,e) Illustration of the reference sample and top view SEM image after heating. f) Schematic illustration of the patterned sample with the PDMS cast. g) Top and tilted view SEM images of the patterned samples with a lattice parameter $a = 600$ nm.

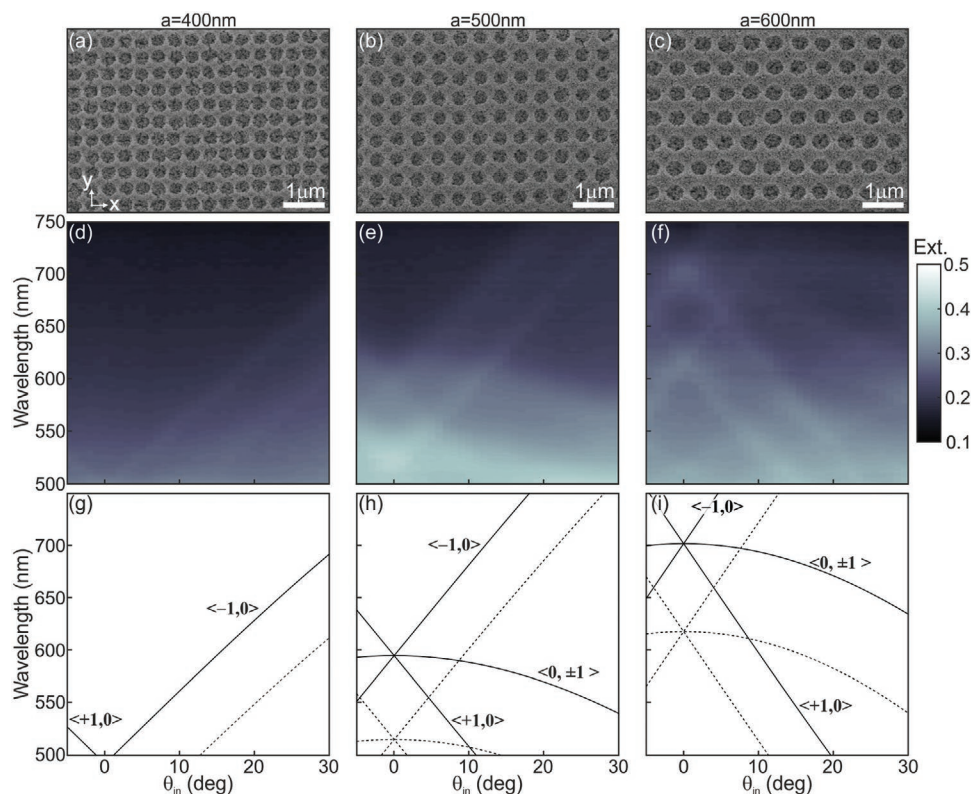


Figure 2. a–c) SEM images for different lattice parameter of the top view ($a = 400, 500,$ and 600 nm, respectively). d–f) Extinction spectra as a function of the incident angle of the patterned samples in (a–c), respectively. g–i) Curves correspond to the RAs calculated for the diffracted beams. Solid curves represent the diffraction associated to the higher effective refractive index and dashed lines represent the diffraction associated to the lower effective refractive index.

yield (PLQY), and PL lifetime) of the phosphor layers, since it improves the crystallinity and eliminates quenching pathways caused by organic groups in the surface of the nanoparticles. After annealing, planar films exhibit a PLQY of 55% (see Experimental Section) and remain transparent in the visible. However, scattering becomes more significant towards the UV. As a result, although nearly full extinction is attained at 285 nm, the absorbance in the UV stays around 50% of the incident light. Figure 1e,g show top view images obtained using scanning electron microscopy (SEM) of both reference and patterned samples after heating. A tilted view of the sample is also shown in Figure 1g.

We patterned the surface of phosphor films with arrays of holes with different lattice parameters, i.e., $a = 400, 500,$ and 600 nm. Lower magnification SEM images of these patterned films are shown in Figure 2a–c. The film with the smallest features ($a = 400$ nm, hole diameter = 296 nm) illustrates how the limit in the resolution of the imprinted features is imposed by the crystal size of the phosphor (in our case, 35 nm). The optical extinction as a function of the angle of incidence (θ_{in}) for the three samples with different lattice parameter is shown in Figure 2d–f. The extinction is defined herein as $1 - T_0$, with T_0 being the zeroth-order transmission. For this measurement, the samples were mounted on a rotation stage and illuminated with a focused beam of unpolarized white light. The sample is rotated θ_{in} with respect to the surface normal along the $y = 0$ plane. At $\theta_{in} = 0^\circ$, we can find the maximum in extinction,

which shifts to longer wavelengths as the lattice parameter is increased. In particular, for a period of 400 nm, two extinction maxima are found at $\lambda = [412, 492]$, while, for the 500 and 600 nm pitches, maxima were detected at $\lambda = [515, 595]$ nm and $\lambda = [615, 700]$ nm, respectively. Here, we fit the observed angular dispersion of the transmittance at $\theta_{in} = 0^\circ$, to that of the estimated RAs. These RAs satisfy the following Equation (1) for the conservation of the wavevector parallel to the plane of the array

$$\vec{k}_{sc,\parallel} = \vec{k}_{in,\parallel} + \vec{G}(m_x, m_y) \quad (1)$$

with $\vec{k}_{sc,\parallel}$ and $\vec{k}_{in,\parallel}$ being the parallel component of the scattered and incoming wavevectors, respectively, and \vec{G} the reciprocal lattice vector, $\vec{G} = 2\pi(m_x/a, m_y/a)$, where a is the lattice constant of the square array and the pair of integers (m_x, m_y) defines the diffraction order. We identified the first diffraction orders reflected into air that matched the experimental values (Figure 2d–f) as the $\langle \pm 1, 0 \rangle$ and $\langle 0, \pm 1 \rangle$ for the two sets of RAs observed (solid and dashed lines in Figure 2g–i). The fitting for the high energy RAs (dashed lines) results in an air-like refractive index ($n_{eff} = 1.03$), while the lower energy RAs (solid lines) can be associated to diffraction at the top of the nanophosphor structure, with the values of the effective index found around 1.2, between the refractive index of the nanophosphor layer and that of air, namely $n_{eff} = 1.23, 1.19,$ or 1.17 for $a = 400, 500,$ and 600 nm, respectively. Slight variations in the hole size or depth

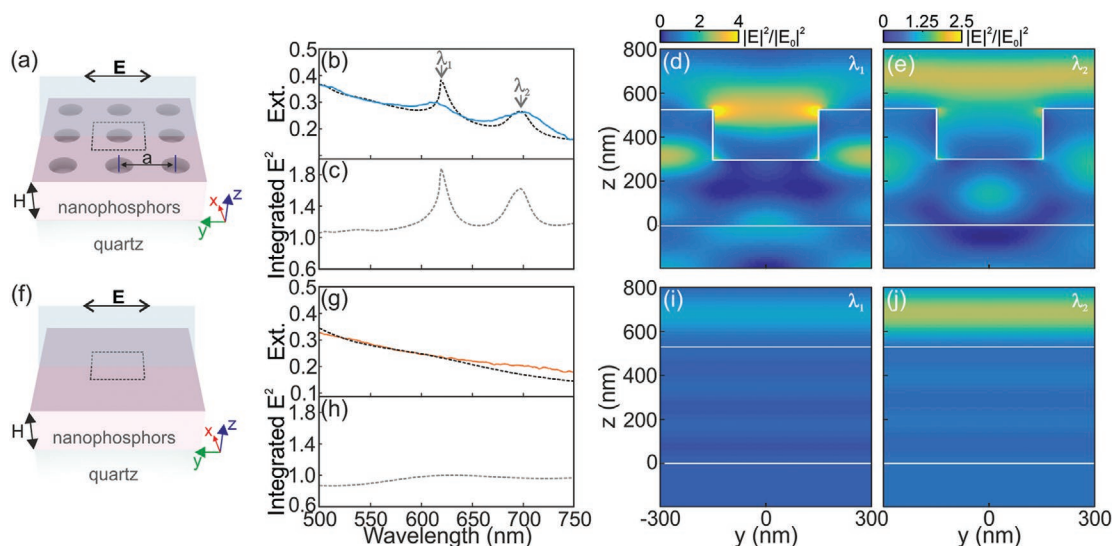


Figure 3. a,f) Illustrative schemes of the simulated structures. b–e) FDTD calculations of the structure with the lattice parameter $a = 600$ nm and g–j) the reference. b,g) Calculated (dashed lines) and experimental (solid lines) extinction. The spectral positions of the maxima in extinction of the patterned sample are tagged with arrows ($\lambda_1 = 619$ nm and $\lambda_2 = 696$ nm). Electric field intensity profile along the plane $X = 0$ of the d,e) patterned and i,j) flat samples at the wavelengths d,i) λ_1 and e,j) λ_2 . c,h) Integrated electric field intensity in the entire volume of nanophosphors normalized to the maximum value for the reference.

for different imprints may bring about small field intensity distribution variations, which result in the different effective refractive indices reported.

Further insight in the field distribution of the RA supported by the nanophosphor gratings is obtained by looking at the spatial distribution of the electric field intensity, $|E|^2$, as well as the absorptance of light impinging normally to the sample. We collected the ballistic transmission from planar and the patterned samples ($a = 600$ nm) and reproduced these curves using the FDTD method. Schemes of both patterned and flat films can be found in **Figure 3a,f** indicating the polarization of the incoming field (E) and the main structural parameters (period, a , and film height, H). For the simulations, we assume a Cauchy spectral dependence of the effective refractive index for the nanophosphor film, with 1.75 at 619 nm, which is a consequence of the high porosity (31%, according to Bruggeman effective medium approximation and considering 2.1 is the index of the bulk material) that nanoparticle-based films feature. The calculated extinction at normal incidence ($\theta_{in} = 0^\circ$) is depicted in **Figure 3b,g** for the patterned film and the reference, respectively. The 0° cut of the experimental measurements are also plot as solid lines. From the comparison, it can be seen that the calculated local maxima of the extinction match well the spectral positions observed experimentally. Also, the YZ plane profile of $|E|^2$ in the nanophosphor layer is plotted as color maps in **Figure 3d,e,i,j**, for those wavelengths at which maximum extinction is detected in **Figure 3b** ($\lambda_1 = 619$ nm and $\lambda_2 = 696$ nm). In **Figure 3c,h**, we plot the value of the $|E|^2$ integrated over the entire volume occupied by the nanophosphors. In the field profiles, the estimated field enhancement in the active layer for both frequencies is roughly twice the values observed for the reference layer. If we consider at this point the reciprocity principle, which allows exchanging the positions of source and receiver, then we can expect an improvement in the out-coupling of these wavelengths when emitted from inside the samples.

In order to study the effects of the photonic architecture on the emission from the phosphor films, we performed angle dependent PL measurements. We carried out two different angular experiments which provide complementary information. First, we mounted the sample in a double goniometer. The two angular degrees of freedom for the sample and the collection system allows us to control both the excitation and the emission angles independently. The excitation source consisted of a 285 nm LED focused in the sample surface and fixed at 40° respect to the sample surface normal, while the detection system was a mobile arm rotating around the sample. **Figure 4a–d** shows the angular measurement of the PL from the different samples. The emission spectra collected along the direction normal to the sample surface ($\theta_{emi} = 0^\circ$) for the flat and patterned samples is shown in **Figure 4a**. The radiative coupling to free space for the most intense peak of the Eu^{3+} cation (619 nm) is enhanced twofold for the patterned film with the larger pitch ($a = 600$ nm) in good agreement with the values of the integrated intensity of the electric field shown in **Figure 3**. In fact, the intensity enhancement observed should be interpreted only as directional emission enhancement because patterning does not alter the fraction of light absorbed by the films at the excitation wavelength (see **Figure S1** and **Table S1**, Supporting Information). The panels in **Figure 4b–d** shows the ratio between the PL of the patterned samples and the reference between $\theta_{emi} = 0^\circ$ and $\theta_{emi} = 30^\circ$. All the features observed are correlated with those shown in the extinction measurements and are associated to the diffracted orders calculated previously. Solid and dashed lines indicating the RAs are included in **Figure 4b–d** to pinpoint the origin of the enhancement of the emission lines of the Eu^{3+} in the patterned samples respect to the flat one observed at specific directions. Fourier images of the unpolarized red emission are shown in **Figure 4e–i**. The samples were mounted in a microscope-based setup and excited through the substrate with the UV source. The numerical

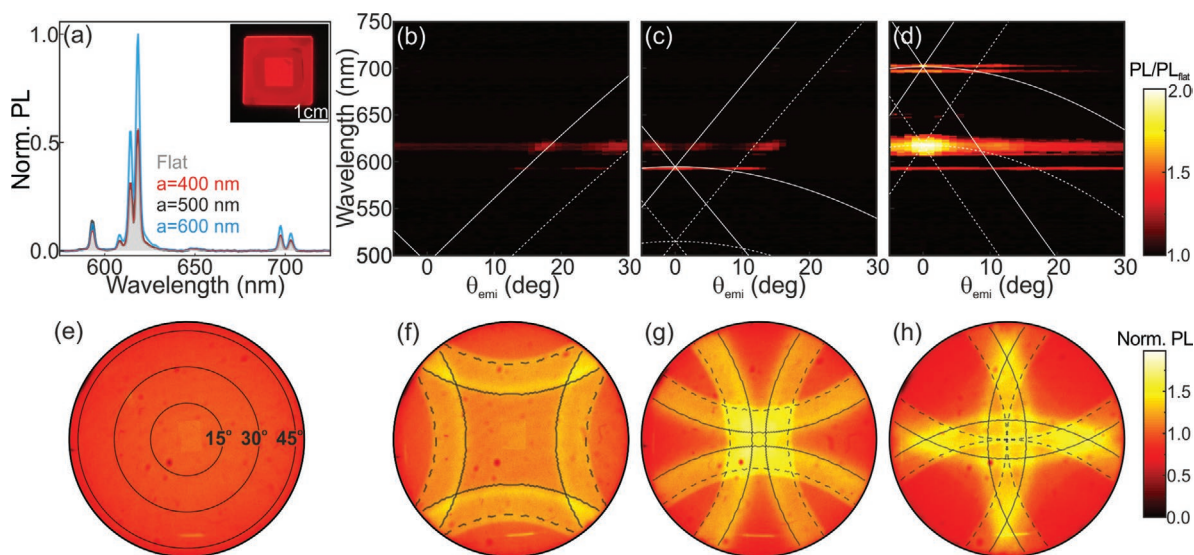


Figure 4. a) Normal direction emission of the reference (gray) and patterned samples: $a = 400$ nm (red), $a = 500$ nm (black), and $a = 600$ nm (blue). The inset shows a picture taken from a sample under the illumination of a UV lamp. Notice that only the $1\text{ cm} \times 1\text{ cm}$ central area of the sample is patterned. b–d) PL enhancement as a function of the emission angle for the different lattice parameters (400, 500, and 600 nm, respectively). e–h) Fourier images of the unpolarized red emission ($\lambda > 619$ nm) of the e) reference, and f–h) nanostructured samples ($a = 400$, 500, and 600 nm, respectively). Curves correspond to the RAs calculated for the beams diffracted. Solid and dashed lines represent the diffraction curves corresponding to the higher and lower effective refractive indexes, respectively.

aperture $\text{NA} = 0.75$ determined the maximum detectable angle ($\theta_{\text{emi}} \approx 48.6^\circ$) and a bandpass filter was used to block the yellow emission and target the most intense red peak (associated to the ${}^5\text{D}_0$ - ${}^7\text{F}_2$ transition). Please note that the previous measurements, shown in Figure 4b–d, correspond to a horizontal (or vertical due to symmetry) cut in the Fourier images displayed in Figure 4e–h. The flat sample (Figure 4e) shows no angular features, as expected for a Lambertian-like emitter. However, patterned films exhibit bands of improved directional emission that follow the dispersion of the RAs (Figure 4f–h). In particular, 400 nm-pitch patterns result in directional sideward emission whereas 600 nm allows beaming of the emission in the normal direction. Fourier analysis highlights the potential of surface patterning to tailor the directionality of the emission of thin phosphor films, being the angle at which the maximum PL directional enhancement is reached controlled with the lattice constant of the pattern.

Notice that directional sideward emission is key, for example, for the development of small bright and directional sources required for the efficient injection of light in a light guide.

Further, we measured the PL decay dynamics by multi-channel scaling (MCS, see Experimental Section). The excited-state lifetime of the emitters is not expected to be modified by the patterning, since no significant change in the local density of photon states occurs as a result of the 2D grating imprinted onto the surface of the nanophosphor film. A two-exponential model is employed to describe the PL dynamics of nanophosphors to account for the different decay rates expected for RE cations located in the bulk or close to the surface of each nanoparticle. The analysis shows that the average lifetime of the Eu^{3+} transitions is found to be similar to that of the flat sample (1.39 ± 0.02 ms). Besides, our results indicate that the main contribution to the average lifetime (around 90%) comes

from the shorter rate associated to cations that sit in the bulk. This confirms that 1) our patterning process does not degrade the emission of the phosphor; and 2) the directional emission enhancement displayed in Figure 3 is only due to the efficient funnelling of the emitted light in particular directions. PL decay curves are available in the supporting information (Figure S2, Supporting Information), along with the corresponding fittings (Table S2, Supporting Information). Consistently, the PLQY remains constant, within experimental error, with respect to the value attained for the reference samples. Flat films show emitted-to-absorbed photon efficiencies of 55%, while the yields of patterned ones are 56%, 56%, and 54% for the lattice parameters 400, 500, and 600 nm, respectively. Our results indicate that 600 nm-pitch patterning provides a redirection of the emitted light that results in a higher fraction of the emitted light in a solid angle close to the normal to the surface respect to a flat reference layer whose emission is Lambertian. Therefore, optical modes supported by the patterned film render the nanophosphor layer into a directional light source, being such directionality controlled by the lattice parameter of the periodic pattern.

We have demonstrated that direct nanoimprinting of nanophosphor layers with 2D square arrays endows the patterned film with enhanced emission at selected wavelengths and directions. Our nanophosphor pastes produce transparent and moldable films that allow the development of a RE-based photonics that could be eventually be put into practice to build more efficient and functional solid-state light emitting devices. Our approach overcomes the limitations imposed by the large crystal size of phosphor crystals employed in conventional color-converting layers resulting in high quality and large area photonic architectures. A twofold enhancement of the emission intensity at certain directions is attained without compromising

the absorption of the film or the efficiency of the emitters, which remains as high as in the standard flat reference film, and employing inexpensive procedures amenable of mass production.

Experimental Section

Materials: Materials used in this study were gadolinium(III) nitrate hexahydrate ($\text{Gd}(\text{NO}_3)_3 \cdot 6\text{H}_2\text{O}$, Aldrich, 99.9%), europium(III) nitrate pentahydrate ($\text{Eu}(\text{NO}_3)_3 \cdot 5\text{H}_2\text{O}$, Aldrich, 99.9%), sodium orthovanadate (Na_3VO_4 , Aldrich, 99.9%), poly(acrylic acid) (PAA, Aldrich, average Mw \approx 1800), ethylene glycol (EG), α -terpineol (SAFC, \geq 96%), ethyl cellulose (Sigma-Aldrich, powder), hard PDMS silicone elastomer kit (Gelest), soft-PDMS (SYLGARD 184, Dow Corning), and 1H,1H,2H,2H-perfluorooctyltrichlorosilane (PFOTS, Alfa Aesar by Thermo Fisher, 97%). Prepatterned silicon masters were purchased from Cemitec (Navarra, Spain).

Nanophosphor Synthesis: Synthesis of $\text{GdVO}_4:\text{Eu}^{3+}$ nanophosphor was performed following a solvothermal method previously reported.^[27] Eu^{3+} concentration was fixed at 10% ($\text{Gd}_{0.9}\text{VO}_4:\text{Eu}^{3+}_{0.1}$). Briefly, uniform NPs were obtained through homogeneous precipitation reaction from the RE precursors and sodium orthovanadate in EG/water mixture at 120 °C. PAA was added during the synthesis as functionalization agent. As a result, sized-controlled nanophosphors with colloidal stability dispersed in methanol were attained.

Paste Preparation: Nanophosphor paste was prepared from the synthesized nanophosphor suspended in methanol. The procedure was suited from the recipe of TiO_2 nanoparticles for electrodes in dye-sensitized solar cells.^[28] In particular, ethyl cellulose was used as organic binder and α -terpineol as solvent. The very same process was reported previously for the vanadate-based nanoparticles presented here.^[5] After the distillation of the methanol in a rotary evaporator, a viscous paste was obtained.

PDMS Mold: PDMS molds were fabricated following a previously reported protocol.^[29] Briefly, silicon masters were functionalized with PFOTS as an anti-sticking layer, lowering the surface energy and allowing the easy release of cured PDMS. The molds were fabricated by casting a thin layer of hard-PDMS on the master followed by a thick layer of soft PDMS as support. The 1 cm² patterns used in this work consist of square arrays of cylindrical pillars with 300 nm diameter; 350 nm height; and lattice parameters of 400, 500, and 600 nm.

Deposition and Nanoimprinting: The viscous paste was diluted in ethanol (1:2 wt) in order to facilitate the spin coating deposition of homogenous films. After the deposition, ethanol was not evaporated yet and the viscosity allowed the patterning. Thus, the imprinting was done right after coating the substrate. Both the reference (flat) and patterned samples were dried for 1 min in a hotplate at 80 °C in order to complete the evaporation of the ethanol. Finally, the samples were annealed at 500 °C with a heating ramp of 10 °C min⁻¹ and a plateau for 2 h. The upper limit of 500 °C in the temperature ensures the organic compounds removal and, at the same time, the nanoparticle size preservation, i.e., it avoids the sintering and deformation of the patterning that we can find for larger temperature treatments. The heating process results in rigid samples and the removal of any organic compound from the paste recipe or the synthesis procedure. The patterned surface area extends to 1 cm².

Structural Characterization: The shape of the nanoparticles was examined by TEM (Philips 200CM). SEM images were taken by using a microscope Hitachi S4800 and a Quanta FEI 200 FEG-ESEM microscope operating at 5 and 10 kV, and secondary and backscattered electrons were detected in a high-vacuum regime (10⁻³ Pa).

Optical Characterization: The excitation and emission spectra, the time-dependent PL intensity, and the PLQY of these samples were measured with an Edinburgh FLS1000 spectrofluorometer. Time-dependent PL measurements were registered for the most intense Eu^{3+} emission band at 619 nm, using a MCS method and a pulsed xenon flashlamp at repetition rate of 50 Hz in a FLS1000 Edinburgh

spectrofluorometer. Temporal resolution was set to 10 μs . Absolute PLQY measurements were performed based on a photon number ratio using an integrating sphere. In fact, PLQY values were obtained from the ratio between light emitted and light absorbed by the different samples. To estimate the fraction of light absorbed by the layers, the scattering of each sample at the excitation wavelength was compared with that of an uncoated quartz substrate used as reference sample. Both sample and reference are placed inside the integrating sphere over a scattering plug made from the same material used for the inner coating of the integrating sphere. The excitation wavelength was set to 285 nm with 10 nm bandwidth and the emission/scattering spectra were measured throughout the excitation and emission spectral ranges, i.e., from 250 to 850 nm, with 0.5 nm bandwidth. Thus, measurements comprise the absorption of UV light by the vanadate matrix, the transfer to Eu^{3+} emitting centers, and the subsequent outcoupling of the emitted light. It is also noteworthy that we checked PLQY values for different excitation wavelengths between 275 and 325 nm and confirmed that our results do not depend on the pumping wavelength within the experimental uncertainty of these measurements (<2%).

The angular-dependent ballistic transmittance and PL of nanophosphor films were recorded in an optical table with a double rotation stage setup using as incident beam a halogen lamp (Ocean Optics HL-2000-HP-FHSA) and 285 nm LED (FWHM = 13 nm, power = 50 mW), respectively. Transmitted and emitted light was detected with a fiber-coupled spectrophotometer (Ocean Optics USB2000+VIS-NIR-ES). Fourier images were measured using a back focal plane microscope with an objective with 0.75 numerical aperture and a CCD camera. The spectral information was obtained with a bandpass filter.

Calculations: FDTD numerical simulations were carried out by means of a commercial software (Lumerical) following the geometrical parameters from the experimental micrographs.

Supporting Information

Supporting Information is available from the Wiley Online Library or from the author.

Acknowledgements

This project received funding from the Spanish Ministry of Economy and Competitiveness under grant MAT2017-88584-R (AEI/FEDER, UE) and PID2019-106860GB-I00 (AEI/FEDER, UE), the excellence program SEV-2015-0496, and the European Research Council (ERC) under the European Union's Horizon 2020 Research and Innovation Programme (NANOPHOM, grant agreement no. 715832 and ENLIGHTMENT, grant no. 637116). P.M acknowledges financial support from an FPI contract (2017) of the MICINN (Spain) cofounded by the ESF and the UAB. E.C.O. acknowledges the Spanish Ministry of Universities for the funding through an FPU program (FPU19/00346).

Conflict of Interest

The authors declare no conflict of interest.

Keywords

color converters, nanoimprinting, nanophotonics, photoluminescence enhancement, rare-earth nanophosphors, soft-lithography

Received: September 17, 2020

Revised: November 4, 2020

Published online:

- [1] Y. Sun, S. R. Forrest, *J. Appl. Phys.* **2006**, *100*, 073106.
- [2] E. Wrzesniewski, S. H. Eom, W. Cao, W. T. Hammond, S. Lee, E. P. Douglas, J. Xue, *Small* **2012**, *8*, 2647.
- [3] J. Y. Oh, J. H. Kim, Y. K. Seo, C. W. Joo, J. Lee, J. I. Lee, S. Yu, C. Yun, M. H. Kang, B. H. Choi, Y. H. Kim, *Dyes Pigment* **2017**, *136*, 92.
- [4] J. M. Miranda-Muñoz, G. Lozano, H. Míguez, *Adv. Opt. Mater.* **2017**, *5*, 1700025.
- [5] J. M. Miranda-Muñoz, D. Geng, M. E. Calvo, G. Lozano, H. Míguez, *J. Mater. Chem. C* **2019**, *7*, 267.
- [6] W. H. Koo, S. M. Jeong, F. Araoka, K. Ishikawa, S. Nishimura, T. Toyooka, H. Takezoe, *Nat. Photonics* **2010**, *4*, 222.
- [7] A. Revaux, G. Dantelle, D. Decanini, F. Guillemot, A. M. Haghiri-Gosnet, C. Weisbuch, J. P. Boilot, T. Gacoin, H. Benisty, *Nanotechnology* **2011**, *22*, 365701.
- [8] S. Wu, H. Xia, J. Xu, X. Sun, X. Liu, *Adv. Mater.* **2018**, *30*, 1803362.
- [9] G. Lozano, D. J. Louwers, S. R. Rodríguez, S. Murai, O. T. Jansen, M. A. Verschuuren, J. G. Rivas, *Light: Sci. Appl.* **2013**, *2*, e66.
- [10] S. Pimputkar, J. S. Speck, S. P. DenBaars, S. Nakamura, *Nat. Photonics* **2019**, *3*, 180.
- [11] P. M. Pattison, J. Y. Tsao, G. C. Brainard, B. Bugbee, *Nature* **2018**, *563*, 493.
- [12] O. Sánchez-Sobrado, M. E. Calvo, N. Núñez, M. Ocana, G. Lozano, H. Míguez, *Nanoscale* **2010**, *2*, 936.
- [13] L. Devys, G. Dantelle, A. Revaux, V. Kubytzky, D. Paget, H. Benisty, T. Gacoin, *Adv. Opt. Mater.* **2014**, *2*, 81.
- [14] S. Gorsky, R. Zhang, A. Gok, R. Wang, K. Kebede, A. Lenef, M. Raukas, L. Dal Negro, *APL Photonics* **2018**, *3*, 126103.
- [15] N. V. Hoang, A. Pereira, H. S. Nguyen, E. Drouard, B. Moine, T. Deschamps, R. Orobtcouk, A. Pillonnet, C. Seassal, *ACS Photonics* **2017**, *4*, 1705.
- [16] D. Geng, G. Lozano, M. E. Calvo, N. O. Núñez, A. I. Becerro, M. Ocaña, H. Míguez, *Adv. Opt. Mater.* **2017**, *5*, 1700099.
- [17] D. Geng, E. Cabello-Olmo, G. Lozano, H. Míguez, *Mater. Horiz.* **2018**, *5*, 661.
- [18] D. Geng, E. Cabello-Olmo, G. Lozano, H. Míguez, *ACS Photonics* **2019**, *6*, 634.
- [19] J. J. Wierer, A. David, M. M. Megens, *Nat. Photonics* **2009**, *3*, 163.
- [20] E. Khaidarov, Z. Liu, R. Paniagua-Domínguez, S. T. Ha, V. Valuckas, X. Liang, Y. Akimov, P. Bai, C. E. Png, H. V. Demir, A. I. Kuznetsov, *Laser Photonics Rev.* **2020**, *14*, 1900235.
- [21] Y. C. Lee, H. L. Chen, C. Y. Lu, H. S. Wu, Y. F. Chou, S. H. Chen, *Nanoscale* **2015**, *7*, 16312.
- [22] Y. Xia, G. M. Whitesides, *Annu. Rev. Mater. Sci.* **1998**, *28*, 153.
- [23] A. Espinha, C. Dore, C. Matricardi, M. I. Alonso, A. R. Goñi, A. Mihi, *Nat. Photonics* **2018**, *12*, 343.
- [24] C. Matricardi, J. L. García Pomar, P. Molet, L. A. Pérez, M. I. Alonso, M. Campoy Quiles, A. Mihi, *Adv. Opt. Mater.* **2020**, *8*, 2000786.
- [25] C. López-López, S. Colodrero, A. Jiménez-Solano, G. Lozano, R. Ortiz, M. E. Calvo, H. Míguez, *Adv. Opt. Mater.* **2014**, *2*, 879.
- [26] P. Molet, L. K. Gil-Herrera, J. L. García Pomar, N. Caselli, A. Blanco, C. López, A. Mihi, *Nanophotonics* **2020**, *9*, 943.
- [27] N. O. Nuñez, S. Rivera, D. Alcantara, J. M. De la fuente, J. García-Sevillano, M. Ocaña, *Dalton Trans.* **2013**, *42*, 10725.
- [28] Y. J. Kim, M. H. Lee, H. J. Kim, G. Lim, Y. S. Choi, N. G. Park, K. Kim W. I. Lee, *Adv. Mater.* **2009**, *21*, 3668.
- [29] T. W. Odom, J. C. Love, D. B. Wolfe, K. E. Paul, G. M. Whitesides, *Langmuir* **2002**, *18*, 5314.